Acta Crystallographica Section D
**Biological Crystallography**
ISSN 0907-4449

# Structure of the small GTPase Rab27b shows an unexpected swapped dimer

**Leonard M. G. Chavas,[a] Seiji Torii,[b] Hironari Kamikubo,[c] Masato Kawasaki,[a] Kentaro Ihara,[a] Ryuichi Kato,[a] Mikio Kataoka,[c] Tetsuro Izumi[b] and Soichi Wakatsuki[a]***

[a]Structural Biology Research Center, Photon Factory, Institute of Materials Structure Science, High Energy Accelerator Research Organization (KEK), Tsukuba, Ibaraki 305-0801, Japan, [b]Department of Molecular Medicine, Institute for Molecular and Cellular Regulation, Gunma University, Maebashi 371-8512, Japan, and [c]Graduate School of Materials Science, Nara Institute of Science and Technology, Ikoma, Nara 630-0192, Japan

Correspondence e-mail: soichi.wakatsuki@kek.jp

Received 16 February 2007
Accepted 20 April 2007

**PDB References:** Rab27b–GDP, $P6_522$, 2iey, r2ieysf; $C2$, 2iez, r2iezsf; $P2_12_12_1$, 2if0, r2if0sf.

Members of the Rab family of small GTPases regulate membrane traffic within the cell by recruiting their specific effectors in a nucleotide-dependent manner. The Rab27 subfamily consists of Rab27a and Rab27b, which share 70% sequence identity. By interacting with a large set of effector proteins such as melanophilin and granuphilin, both Rab27a and Rab27b regulate the exocytosis of secretory lysosomes. Here, the crystal structures of mouse Rab27b in complex with GDP have been determined in three distinct crystal lattices. Surprisingly, Rab27b–GDP exists in an open conformation with protruding switch and interswitch regions, which are stabilized through dimerization by means of domain-swapping in the crystals. In contrast, small-angle X-ray scattering measurements showed an extended monomer form of Rab27b in solution. The observed dimer formation of Rab27b–GDP in the crystals would restrain the highly flexible switch regions. Possible biological implications of this atypical structure of Rab27b and its plausible influence in effector interaction are discussed.

## 1. Introduction

Regulation of cellular functions such as membrane trafficking, cell growth and cytoskeletal dynamics is partly mediated by members of the Ras superfamily of small GTPases. These proteins function as molecular switches that cycle between inactive GDP-bound and active GTP-bound conformations and recruit their specific effector proteins while in their active state. Within the Ras superfamily, Rab GTPases form the largest family, with over 60 members (Pereira-Leal & Seabra, 2000), and mediate the tethering of transport vesicles to discrete cellular compartments (Zerial & McBride, 2001).

In the past few years, an increasing number of structural analyses of Rabs, either alone or in complex with effector and regulator proteins, have provided valuable insights into their distinct methods of mediating diverse cellular processes (Pfeffer, 2005). Rab geranylgeranyl transferase (GGTase) modifies newly synthesized cytosolic Rabs by attaching geranylgeranyl groups to a conserved dicysteine motif in the C-terminus (Zhang *et al.*, 2000). Prenylated Rabs are then carried to their respective target membranes by Rab escort protein (REP), which also appears to be critical in the prenylation step (Rak *et al.*, 2004). At the target membrane, guanine nucleotide-exchange factors (GEFs) catalyze the exchange of GDP for GTP to turn on the GTPase (Itzen *et al.*,

2006). Activated Rabs subsequently interact with downstream effectors to convey vesicles to their proper docking site at the acceptor membrane (Ostermeier & Brunger, 1999; Zhu *et al.*, 2004; Eathiraj *et al.*, 2005; Kawasaki *et al.*, 2005). Different Rabs recognize specific partner proteins by modulating their characteristic Rab-subfamily (RabSF) motifs, in addition to the Rab-family (RabF) motifs that cluster in and around the so-called switch I, switch II and interswitch regions (Pereira-Leal & Seabra, 2000). Upon GTP activation, Rabs and their effectors initially interact *via* the switch regions. Additionally, Rab complementary-determining regions (RabCDRs), which include RabSF1, RabSF3 and RabSF4, provide binding specificity for particular sets of partner proteins (Ostermeier & Brunger, 1999; Wu *et al.*, 2005). Interactions between Rabs and their effectors are highly specific, ensuring the proper transport of vesicles to their acceptor membranes. Subsequently, Rabs lose their interaction with effectors upon hydrolysis of GTP, an event that is accelerated by GTPase-activating proteins (GAPs; Rak *et al.*, 2000; Pan *et al.*, 2006). GDP-bound Rabs are extracted from the membrane by Rab GDP dissociation inhibitors (RabGDIs). Rabs bound to RabGDIs are thought to function as a cytosolic pool of inactive Rabs (Pylypenko *et al.*, 2006), which can be recycled back to target membranes upon interaction with GDI displacement factor (GDF; Dirac-Svejstrup *et al.*, 1997).

Several genetic diseases have been ascribed to the dysfunction of Rab regulator proteins (Seabra *et al.*, 2002; Verhoeven *et al.*, 2003). A mutation in the Rab GGTase $\alpha$-subunit causes gunmetal phenotype, a mouse model of Hermansky–Pudlak syndrome (HPS) characterized by partial albinism. Mutations of Rab escort protein 1 (REP1) cause choroideremia (CHM) through photoreceptor-cell degeneration. Furthermore, mutations in RabGDI$\alpha$ are associated with X-linked mental retardation. On the other hand, Rab27a and additionally Rab7 (Verhoeven *et al.*, 2003) are thus far the only examples of Rabs that are related to human diseases. Griscelli syndrome (GS) associates partial albinism and immunodeficiency as a consequence of defects in melanosome transport and granule secretion by cytotoxic T-lymphocytes (Seabra *et al.*, 2002). Three mouse models of GS, ashen, dilute and leaden, are attributed to mutations in Rab27a, myosin Va and melanophilin (also called Slac2-a), respectively.

Rab27a and Rab27b constitute the Rab27 subfamily and share high sequence identity (Fig. 1). Both Rab27 isoforms interact with a large panel of effector proteins (Izumi *et al.*, 2003; Fukuda, 2005) and appear to have similar functions. As exemplified in GS, Rab27a is involved in melanosome transport in melanocytes through the specific recognition of its effector melanophilin. Melanophilin assists melanosome transport by forming a tripartite complex with Rab27a on vesicles and myosin Va on actin filaments (Izumi *et al.*, 2003; Fukuda, 2005). In pancreatic $\beta$-cells, Rab27a cooperates with granuphilin-a (also named Slp4-a) in promoting the plasma-membrane targeting of insulin granules (Izumi *et al.*, 2003; Fukuda, 2005). The expression pattern of the two proteins is partially divergent (Zhao *et al.*, 2002); for example, in brain tissue, where Rab27b is highly expressed, Rab27a is barely detectable.

Here, we report the crystal structure of Rab27b in its GDP-bound state. Surprisingly, unlike the other small GTPase structures reported to date, Rab27b–GDP dimerizes through domain-swapping. Rab27b completely rearranges its switch regions from the canonical conformation to swap two $\beta$-strands in three different crystal forms. The potential role of Rab27b dimerization during its GTPase cycle is addressed.

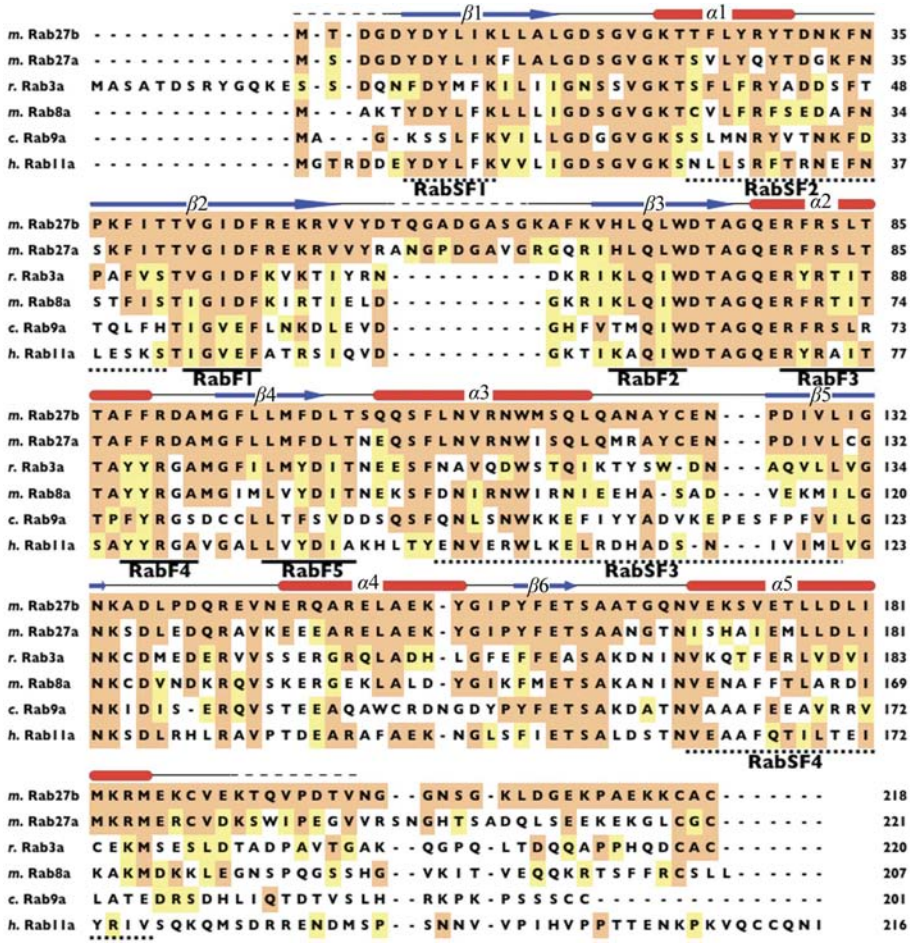


**Figure 1**
Structure-based sequence alignment of several Rab GTPases. Sequence identity between the proteins is highlighted in orange and similarity is highlighted in yellow. Secondary-structural elements are represented by blue arrows and red bars for $\beta$-strands and $\alpha$-helices, respectively. The RabF and RabSF motifs are underlined at the bottom of the sequence alignment. *m.*, *Mus musculus*; *r.*, *Rattus norvegicus*; *c.*, *Canis familiaris*; *h.*, *Homo sapiens*.

## 2. Materials and methods

### 2.1. Cloning, expression, purification and crystallization

The coding region of the mouse Rab27b Gln78Leu mutant was subcloned into pGEX-4T-1 (GE Healthcare) and pET15b (Novagen) vectors and the recombinant protein expressed in *Escherichia coli* BL21(DE3) LysS cells was purified by affinity chromatography using glutathione Sepharose 4B (GE Healthcare) or Ni–NTA nickel-affinity resin (Qiagen) followed by thrombin digestion and size-exclusion chromatography. SeMet-substituted Rab27b Gln78Leu produced by DL41 cells grown in SeMet-containing medium was purified as described above. Although the Rab27 Gln78Leu mutant is known as deficient in GTP hydrolysis, purified Rab27b presents a mixture of GTP- and GDP-bound forms (ratio of 1:4), probably because of its residual intrinsic GTPase activity (our unpublished observation). Hence, nucleotide exchange was performed on glutathione Sepharose 4B resin by extensive washing with a buffer containing 10 m*M* EDTA followed by loading of 5 m*M* GDP with 5 m*M* $Mg^{2+}$. The nucleotide content of the GTPase was confirmed by ion-exchange chromatography of the released nucleotide after heat-denaturing and precipitating the protein. Approximately 25 mg Rab27b–GDP could be obtained from 1 l culture. The purified sample was further dialyzed against 150 m*M* sodium chloride, 1 m*M* magnesium chloride and 20 m*M* Tris pH 8.0 and concentrated to 10 mg $ml^{-1}$.

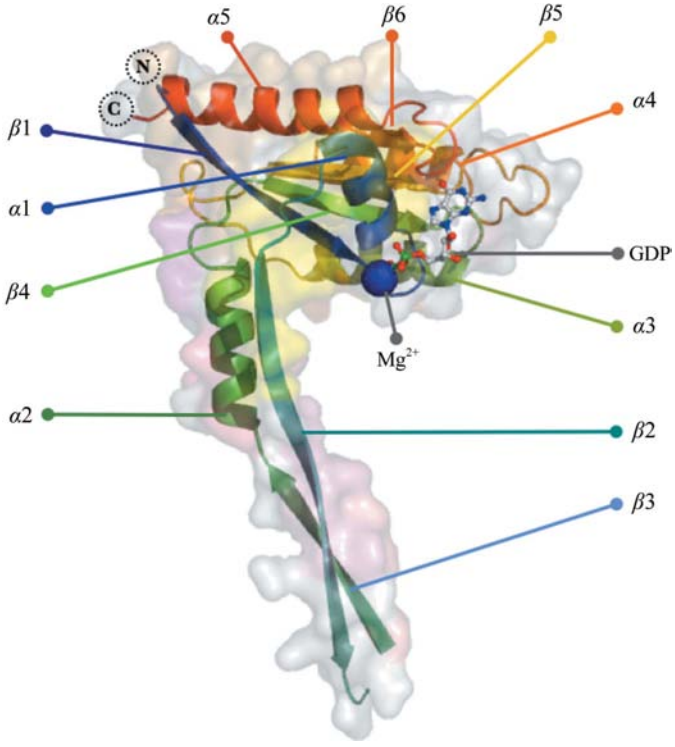


**Figure 2**
Rab27b–GDP monomer structure: a ribbon diagram of the Rab27b–GDP monomer showing individual secondary-structural elements coloured progressively from the N-terminus in blue to the C-terminus in red. GDP and $Mg^{2+}$ are represented as a ball-and-stick model and a sphere, respectively. The N- and C-termini are labelled. The protein surface is also shown in the background.

The GTPase was crystallized in three different space groups using the hanging-drop vapour-diffusion method. Crystals of full-length (residues 1–218) Rab27b diffracted to 8.0 Å resolution. Truncation of the C-terminal flexible region enhanced the resolution to about 3 Å depending on the crystal packing. Hexagonal crystals (space group $P6_522$, unit-cell parameters $a = b = 66.1$, $c = 380$ Å) of Rab27b (residues 1–193) grew in a few days from a reservoir containing 20% polyethylene glycol 10 000 and 100 m*M* Tris buffer pH 7.5 at 293 K in the presence of 5 m*M* dithiothreitol. Monoclinic crystals (space group *C*2, $a = 170.6$, $b = 63.4$, $c = 80.9$ Å, $\beta = 98.4^\circ$) of Rab27b (residues 1–215) appeared after several months from a solution containing 30% 2-methyl-2,4-pentanediol (MPD), 20 m*M* calcium chloride and 100 m*M* HEPES pH 7.0 at 289 K. Orthorhombic crystals (space group $P2_12_12_1$, $a = 55.0$, $b = 64.8$, $c = 153.3$ Å) of Rab27b (residues 1–198) were obtained using 20% MPD and 100 m*M* sodium cacodylate pH 5.5 at 289 K. Initial phases were obtained from the hexagonal crystal, but the best diffraction data were from the orthorhombic lattice.

### 2.2. Data collection, structure determination and refinement

For X-ray diffraction data collection, crystals were flash-cooled in a 100 K dry nitrogen stream, eventually using 20% glycerol as a cryoprotectant (for hexagonal crystals). Diffraction data from the $P6_522$ crystal of SeMet-labelled Rab27b–GDP were recorded on an ADSC Q4R CCD detector at a wavelength of 0.9789 Å on beamline 6A of the Photon Factory (PF). The X-ray intensities were evaluated to 3.2 Å. Initial phases were determined by the single-wavelength anomalous dispersion (SAD) method using the program *SOLVE* (Terwilliger & Berendzen, 1999), which located six Se atoms from the 12 SeMet residues in the asymmetric unit (Supplementary Fig. 1[1]). The asymmetric unit contained two Rab27b molecules, referred to as molecules HA and HB, resulting in a Matthews coefficient of 2.66 $Å^3$ $Da^{-1}$ and a solvent content of 53.8% (Matthews, 1968). Both Rab27b molecules were bound to a GDP, with interpretable electron densities for protein residues 4–54, 66–75 and 83–185 in molecule HA and 5–55, 64–116 and 125–184 in molecule HB. The $P6_522$ crystals of the native Rab27b were not reproducible. Consequently, all the refinements were performed using the SeMet crystals. The cystallographic *R* factor and $R_{free}$ values are 0.289 and 0.346, respectively (Table 1).

Diffraction data were collected from the *C*2 crystals using an ADSC Q315 CCD detector at a wavelength of 1.0000 Å on beamline 5A of the PF. The crystal was flash-cooled directly without additional cryoprotectant. The outer shell resolution was limited to 2.8 Å. Four Rab27b–GDP–($Mg^{2+}$ or $Ca^{2+}$) complexes were identified in the asymmetric unit by the molecular-replacement method using a single Rab27b core domain without the switch regions extracted from the $P6_522$ crystal structure as a search model (Matthews coefficient of

[1] Supplementary material has been deposited in the IUCr electronic archive (Reference: BE5081). Services for accessing this material are described at the back of the journal.

**Table 1**
Data-processing and refinement statistics.

Values in parentheses are for the highest resolution shell.

| | Se derivative | Native 1 | Native 2 |
|---|---|---|---|
| Data collection | | | |
| Space group | $P6_522$ | $C2$ | $P2_12_12_1$ |
| Unit-cell parameters (Å, °) | $a = b = 66.06$, $c = 379.99$ | $a = 170.55$, $b = 63.39$, $c = 80.93$, $\beta = 98.44$ | $a = 54.96$, $b = 64.76$, $c = 153.33$ |
| Wavelength (Å) | 0.9789 | 1.0000 | 1.0000 |
| Resolution (Å) | 63.4–3.2 | 84.2–2.8 | 40.1–2.8 |
| Reflections | 246530 | 58126 | 93323 |
| Unique reflections | 9175 | 11277 | 14413 |
| $R_{merge}$† (%) | 11.1 (69.3) | 10.5 (27.1) | 10.9 (41.8) |
| Completeness (%) | 99.8 (100.0) | 98.1 (93.8) | 99.7 (97.4) |
| $\langle I\rangle/\langle\sigma(I)\rangle$ | 10.8 (8.5) | 8.2 (3.9) | 13.1 (3.3) |
| Phasing statistics | | | |
| FOM | 0.31 | — | — |
| FOM after *RESOLVE* | 0.69 | — | — |
| Refinement | | | |
| Resolution (Å) | 3.2 | 2.8 | 2.8 |
| $R$ factor‡ (%) | 28.9 | 26.2 | 25.9 |
| $R_{free}$‡ (%) | 34.6 | 36.3 | 31.5 |
| R.m.s.d. bond lengths (Å) | 0.009 | 0.008 | 0.008 |
| R.m.s.d. bond angles (°) | 1.181 | 1.189 | 1.067 |
| Average $B$ factors (Å$^2$)/No. of atoms | | | |
| Protein non-H atoms | | | |
| Chain A | 48.3/1337 | 65.1/1448 | 40.6/1420 |
| Chain B | 53.8/1334 | 43.4/1388 | 42.9/1429 |
| Chain H | — | 65.5/1372 | — |
| Chain I | — | 52.9/1392 | — |
| Water molecules | 35.8/11 | 39.5/38 | 24.3/14 |
| Ligand non-H atoms | GDP, 39.8/56 | GDP–$Ca^{2+}$, 45.2/116 | GDP–$Mg^{2+}$, 31.7/58 |
| Φ/Ψ angles (%) | | | |
| Most favoured region | 81.7 | 86.7 | 90.8 |
| Additionally allowed region | 16.6 | 12.8 | 8.9 |
| Generously allowed region | 1.7 | 0.5 | 0.3 |

† $R_{merge} = \sum_h \sum_j |I_j(h) - \langle I(h)\rangle| / \sum_h \sum_j I_j(h)$, where $I_j(h)$ is the $j$th measurement of reflections indices $h$ and $\langle I(h)\rangle$ is the mean intensity. ‡ $R_{factor} = \sum_h ||F_o(h)| - |F_c(h)|| / \sum_h |F_o(h)|$; $R_{free}$ was calculated using 5% of data excluded from refinement.

2.18 Å$^3$ Da$^{-1}$; solvent content 43.7%). The four molecules, termed MA, MB, MH and MI, consist of residues 6–54 and 62–190 in MA, 3–51 and 68–189 in MB, 11–55 and 65–188 in MH and 6–46 and 69–190 in MI. The $R$ factor and $R_{free}$ are 0.262 and 0.363, respectively (Table 1).

The $P2_12_12_1$ crystals diffracted to 2.8 Å resolution on an ADSC Q4R CCD detector on beamline 6A at the PF. The structure was solved by the molecular-replacement method using the coordinates of a monomer from the $C2$ crystal structure. Two molecules of Rab27b–GDP–$Mg^{2+}$, referred to as PA and PB, are arranged in the asymmetric unit (Matthews coefficient of 3.4 Å$^3$ Da$^{-1}$; solvent content 63.0%). The final model consists of residues 6–54 and 65–189 in PA and 6–54 and 65–190 in PB. The $R$ factor and $R_{free}$ values are 0.259 and 0.315, respectively (Table 1).

All diffraction data were integrated and scaled using the *HKL*-2000 suite (Otwinowski & Minor, 1997). Models and all subsequent manual rebuilding were computed on an electron-density map using *Coot* (Emsley & Cowtan, 2004). The initial model was refined using *CNS* (Brünger *et al.*, 1998) and *CCP*4*i* (Potterton *et al.*, 2003). Crystallographic and refinement statistics are summarized in Table 1. The structures were analyzed and compared with other GTPases using programs from the *CCP*4 suite. Figures were drawn using a combination of the programs *PyMOL* (DeLano, 2005) and *GRASP* (Nicholls *et al.*, 1993).

### 2.3. Pull-down assay

GST-tagged Rab27b Glu78Leu was charged onto glutathione Sepharose 4B resin. His-tagged Rab27b was then loaded onto the resin and incubated at 277 K for 12 h, followed by extensive washing. Proteins were eluted with 10 m*M* reduced glutathione, dialyzed and passed through Ni–NTA nickel-affinity resin (Qiagen). Proteins bound to the resin were analyzed by SDS–PAGE.

### 2.4. Immunoprecipitation

COS7 cells were transfected with Rab27b-encoding plasmids using Lipofectamine 2000 reagent (Invitrogen) according to the manufacturer's instructions. 20 h after transfection, cells were harvested and lysed by scraping in lysis buffer (150 m*M* NaCl, 5 m*M* $MgCl_2$, 10 m*M* Tris pH 7.5, 0.2% NP-40, 0.5 m*M* phenylmethylsulfonyl fluoride, 5 µg ml$^{-1}$ aproptin, 5 µg ml$^{-1}$ pepstatin A and 5 µg ml$^{-1}$ leupeptin). Immunoprecipitation with monoclonal antibody (Roche Diagnostics) was performed on clarified lysates at 277 K. Immunoprecipitates and original cell extracts were separated by SDS–PAGE and transferred onto an Immobilon-P membrane (Millipore). Blots were sequentially incubated with anti-GFP mouse monoclonal antibodies (Roche) and with horseradish peroxidase-conjugated secondary antiserum (Jackson Immunoresearch) and were detected using enhanced chemiluminescent Western blotting detection reagents (GE Healthcare).

### 2.5. Dynamic light scattering (DLS)

DLS measurements were performed on a DynaPro-801 TC (Protein Solutions Co.) device employing a 20 mW solid-state laser (λ = 780.0 nm). All data were obtained at a 90° angle at 298 K. The hydrodynamic diameter $d_H$ and the size distribution of the scatterer were calculated from the scattering data using the program provided by the manufacturer of the instrument.

### 2.6. Small-angle X-ray scattering (SAXS)

SAXS measurements were carried out on a Rigaku PSPC detector at a wavelength of 1.4880 Å on beamline 10C of the PF. Various concentrations of protein samples (from 1.37 to 5.56 mg ml$^{-1}$) in 150 m*M* NaCl, 1 m*M* $MgCl_2$, 20 m*M* Tris pH

8.0 were exposed for 5 min at 293 K. Each trace was subjected to a linear fit in the Guinier region ($Q^2 < 0.013$ Å$^{-2}$) to determine the values of the slope ($-R_g^2/3$) and the $y$ intersection {ln[$I(0)$]}. Intrinsic values of $I(0)$/concentration and $R_g^2$ were estimated by linear extrapolation to zero concentration, resulting in 5300 ± 200 and 380 ± 23 Å$^2$, respectively. Using a reference of 10900 ± 750 for $I(0)$/concentration of chicken-egg ovalbumin (45 kDa), the apparent molecular weight of Rab27b–GDP in solution was determined to be 21.9 ± 0.8 kDa. The pair correlation function $P(r)$ was calculated using the *GNOM* program package (Svergun *et al.*, 1995). The $P(r)$ functions of the model structures obtained from the crystal structures were calculated using *CRYSOL* (Svergun & Stuhrmann, 1991) and *GNOM*.

## 3. Results

### 3.1. Structure determinations

Three crystal structures of Rab27b–GDP were solved in three different space groups: $P6_522$, $C2$ and $P2_12_12_1$. Despite the high sequence similarity (39% identical to Rab3a) and conserved folding among Rab GTPases (Fig. 1), no interpretable solution could be obtained by molecular replacement using known Rab structures. Therefore, the initial phases were determined from the hexagonal crystal using the SAD method. Supplementary Fig. 1 shows the locations of the Se atoms in the asymmetric unit in the $F_o - F_c$ difference Fourier map after initial phasing and density modification. The asymmetric unit contains a homodimer of Rab27b molecules, referred to hereafter as HA–HB. The monoclinic crystal structure was solved by molecular replacement using the monomeric core excluding the switch I, switch II and interswitch regions extracted from the $P6_522$ crystal structure as a search model. Two dimers, MA–MB and MH–MI, are present in the asymmetric unit. Because these two dimers are essentially identical, with only minor structural differences in their switch I, switch II and interswitch regions, only MA–MB will be described in detail below. The crystals with the orthorhombic lattice contain one dimer (PA–PB) per asymmetric unit. Initial phases were obtained by the molecular-replacement method using the MA coordinates as a search model. Inspection of the dimer arrangements between symmetry-related molecules in the three different lattices confirms that each space group adopts distinct packing (data not shown).

The elevated values of the crystallographic $R_{free}$ in the case of the $P6_522$ and $C2$ space groups could be a consequence of the low quality of the data collected ($R_{merge}$ of 11.1% and 10.5% at 3.2 and 2.8 Å resolution, respectively) in addition to the high average atomic displacement parameters ($B$ factors of 50.8 and 56.4 Å$^2$, respectively; Table 1). Nevertheless, the phasing statistics from the SAD phasing support the validity of the hexagonal lattice structure.

### 3.2. Overall structure of Rab27b–GDP

Unexpectedly, the crystal structures of Rab27b–GDP in the three different space groups revealed a protrusion of the extended switch I, switch II and interswitch regions (comprising strands $\beta2$ and $\beta3$ and helix $\alpha2$) like an antenna,

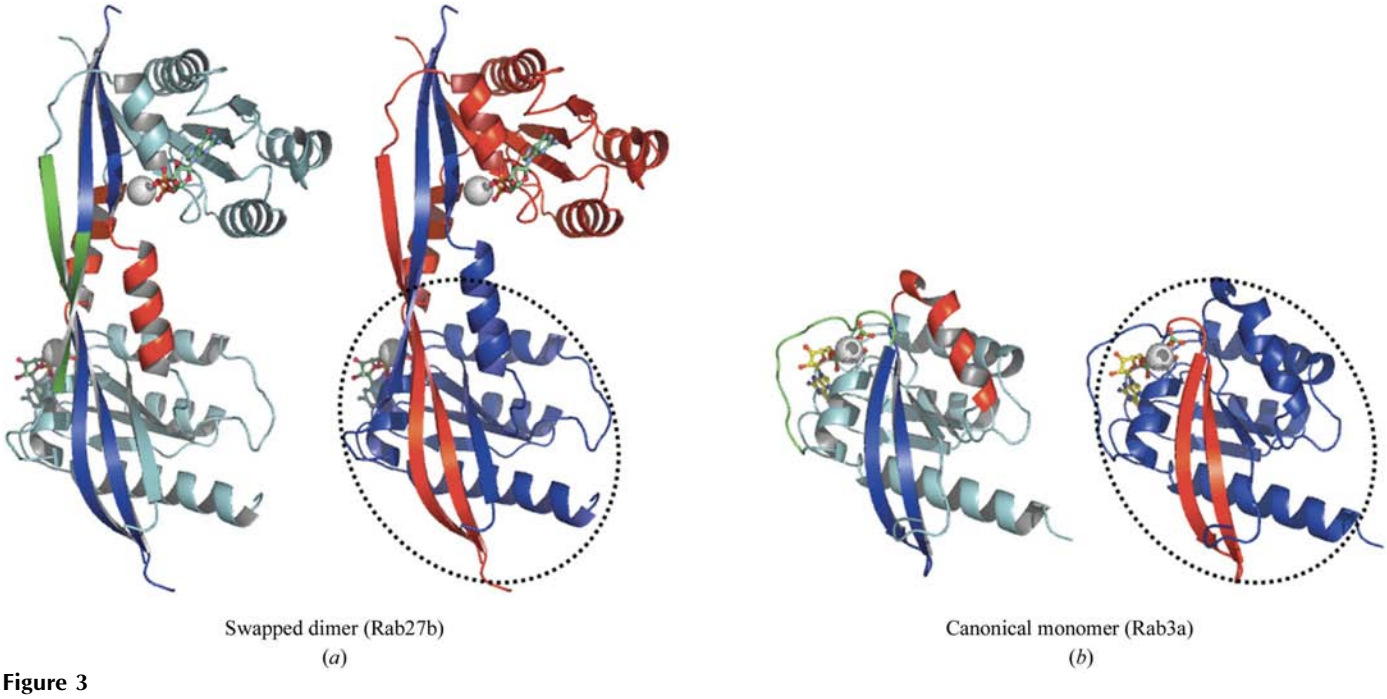


**Figure 3**
Comparison of a domain-swapped Rab27b–GDP dimer with a Rab3a monomer: ribbon diagrams of Rab27b–GDP (*a*) and Rab3a–GPPNHP (PDB code 3rab) (*b*). The left-hand panels are coloured according to the switch I (green), interswitch (blue) and switch II (red) regions. In the right-hand panels, the Rab27b MA (red) and MB (blue) molecules are coloured differently. Rab3a is coloured blue, except for the $\beta2$ and $\beta3$ strands, which are coloured red. The monomeric entity corresponding to the Rab3a monomer is enclosed by a dotted line. The nucleotides and $Mg^{2+}$ are represented as ball-and-stick models and as a sphere, respectively.

creating an intermonomer interface for a domain-swapped dimer (Fig. 2). Superimpositions of the structures of Rab27b with 44 known Rab structures indicate that the GDP-bound Rab27b, both from mouse (our structures) and from human (PDB code 2f7s), is the first to reveal such an extended form of the switch regions, although the core structure of Rab27b without the switch I, switch II and interswitch regions superposes well with the other Rab GTPases with an average r.m.s.d. of 1.40 Å for the main-chain $C^{\alpha}$ positions (1.08 Å for Rab3a; Supplementary Fig. 2). The dimer interfaces extracted from the $P6_522$, $C2$ and $P2_12_12_1$ lattices bury surface areas of 3298, 3064 and 2956 Å$^2$, respectively. The dimerization is characterized by the formation of an antiparallel intermolecular $\beta$-sheet between the long $\beta2$ strands protruding from each of the two monomers (residues Ser36–Phe46). The switch I region, which normally connects helix $\alpha1$ and strand $\beta2$ in the canonical Rab structures, forms the N-terminal half of the unusually long $\beta2$ strand in the Rab27b–GDP structure. Together with the C-terminal half of strand $\beta2$, strand $\beta3$ enters into the neighbouring molecule and makes a swapped interswitch region (Figs. 3*a* and 4). In this arrangement, strand $\beta3$ forms a parallel $\beta$-sheet with strand $\beta1$ of the second molecule. A hydrogen-bonding network between the main-chain atoms of strands $\beta1$, $\beta2$ and $\beta3$ stabilizes the dimer interface (Fig. 5), resulting in a layer of twisted $\beta$-sheets comprised of a total of 12 $\beta$-strands from two monomers (Figs. 3*a* and 4). Adjacent to strand $\beta3$, helix $\alpha2$ folds back to the core domain of the first molecule (Fig. 2). The hydrophobic side of the amphiphilic helix $\alpha2$ packs against the intermolecular $\beta$-sheet. Hydrophobic residues, such as Leu84 and Phe88 of helix $\alpha2$, shape a groove that accepts Ile44 of strand $\beta2$. In the monoclinic and orthorhombic crystals, two dimerized Rab27b molecules are related to each other by a pseudo-twofold symmetry axis between the two Thr41 residues (Fig. 5*b*). Around the pseudo-twofold symmetry, Phe81 of helix $\alpha2$ stacks in a face-to-face interaction. Bridged by the extended strand $\beta2$ and helix $\alpha2$, the core domains of the two protomers are well separated from each other (Fig. 3*a*).

In the present model, RabSF1–4 are exposed to solvent, whereas RabF1–4 are engaged in dimerization, with RabF5 buried in the protein (Fig. 6). Interestingly, and consistent with a role in effector recognition, RabSF1, 3 and 4 (also called RabCDR I, II and III) have elevated temperature factors. Despite the fact that Rab27b–GDP was crystallized in

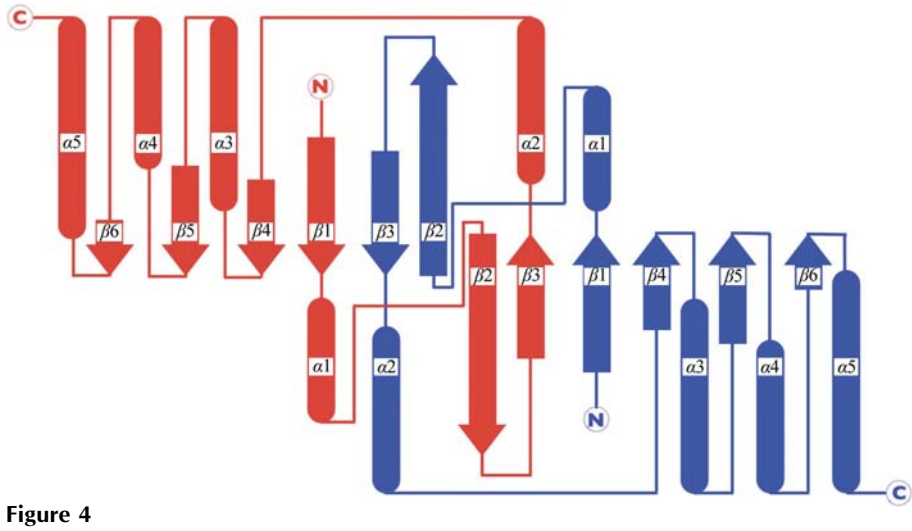


**Figure 4**
Arrangement of Rab27b secondary-structural elements as a topology diagram. Arrows and ovals represent $\beta$-strands and $\alpha$-helices, respectively. The two molecules in the dimer are coloured differently. Individual elements are labelled and the N- and C-termini are indicated.

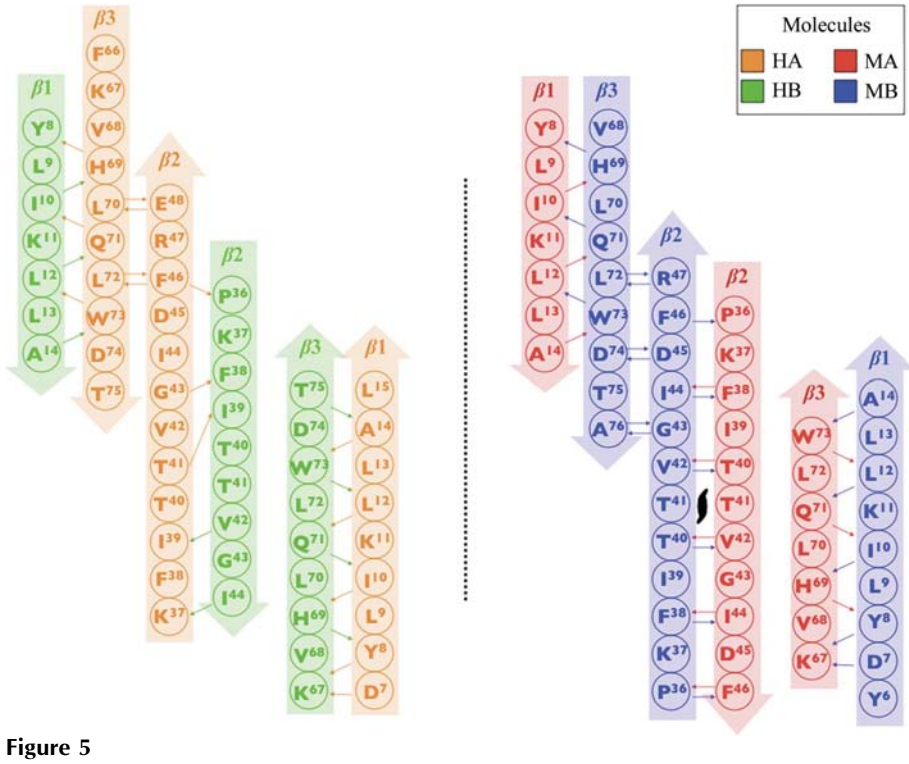


**Figure 5**
$\beta$-Sheet of switch/interswitch regions. Interaction diagram representing the hydrogen-bonding interactions between monomers in the $P6_522$ (*a*) and $C2$ (*b*) lattices. Residues are labelled. Strands are coloured according to the molecule that they belong to. Hydrogen bonds are indicated by arrows from the donor residue to the acceptor residue. A pseudo-twofold axis is marked in the $C2$ arrangement between the two Thr41 residues. The diagram for the $P2_12_12_1$ lattice is identical to that for the $C2$ lattice.

different lattices, the Rab27 subfamily-specific insertion in the $\beta2$–$\beta3$ loop (residues Thr55–Ala65; Fig. 1) is not visible in the electron density, suggesting intrinsic flexibility of this region.

### 3.3. Swapping properties

To be classified as a domain-swapped structure, both contrasting oligomeric and monomeric forms must be known. While the present structures of Rab27b all have dimeric conformations, the previously solved monomeric Rab structures allowed us to define the swapping properties of Rab27b–GDP (Fig. 3). As previously discussed (Bennett *et al.*, 1995), in a swapped structure the oligomer should be assembled by trading a motif that occupies the same environment in the oligomer as it does in the monomer. Consequently, the monomer and oligomer should be stabilized by similar driving forces. In addition, the swapped motif and the rest of the molecule are linked by a so-called hinge loop, which adopts different conformations in the isolated monomer and the swapped oligomer. In our structures, the swapped motif corresponds to the interswitch region, while the hinge loop consists of the N-terminal part of strand $\beta2$ and helix $\alpha2$ (Figs. 3 and 4), which correspond to switch I and switch II, respectively. Furthermore, superimposition of the Rab27b structures from the three distinct lattices reveals some structural deviations in the $\beta2$ strand (Fig. 7). Whereas the three crystal structures share an identical parallel $\beta$-sheet arrangement of the $\beta1$ and $\beta3$ strands, a tilt in the $\beta2$ strand leads to a difference in the hydrogen-bond network interface surrounding it. In contrast to the $C2$ and $P2_12_12_1$ structures, a twisted $\beta2$ strand in the $P6_522$ lattice structure results in fewer hydrogen bonds between the $\beta2$ strands of both monomers (Fig. 5). As a consequence, when the core domains of MA and PA are superimposed on the HA molecule (the r.m.s.d. values are 0.89 and 0.72 Å for the superimposition of MA/HA and PA/HA core domains, respectively), the equivalent MB and PB molecules do not fit on HB, but are tilted by about 33° with respect to each other (Fig. 7). This mismatch, together with the elevated temperature-factor values, reflects the intrinsic flexibility of the switch I, switch II and interswitch regions in contrast to the core domain of the GTPase. It is noteworthy that prolines are often located in the hinge loops of swapped proteins and are thus considered as the critical kink for hinge-loop flexibility (Liu & Eisenberg, 2002). Accordingly, one proline (Pro36) is present at the N-terminus of the $\beta2$ strand of Rab27b (Fig. 1) and is followed by $\beta2$-strand residues that show large conformational deviations (Fig. 7). In contrast, Pro36 of Rab27b is absent in Rab27a (Fig. 1). It would be interesting to verify whether the Rab27a isoform also exhibits core-swapping upon GDP binding or whether this atypical folding is unique to Rab27b.

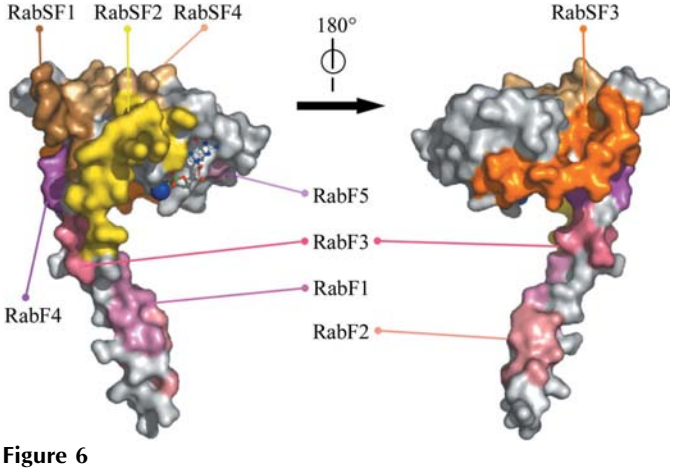


**Figure 6**
Locations of RabF and RabSF motifs. Molecular-surface representation of Rab27b coloured according to the labelled RabF and RabSF motifs. The left-hand panel is in the same orientation as in Fig. 2; the right-hand panel is rotated by 180° around the vertical axis.

### 3.4. Biochemical analyses

We investigated whether Rab27b–GDP forms a dimer under physiological conditions using various biochemical assays. Because the protein eluted as a monomer on size-exclusion chromatography (Supplementary Fig. 3), we assessed possible homodimerization in solution using pull-down assays. No signal indicating Rab27b dimerization could be observed from an *in vitro* experiment using purified GST-tagged and His-tagged Rab27b–GDP (Supplementary Fig. 4). To evaluate their interaction in mammalian cells, we co-expressed HA- and EGFP-tagged Rab27b wild type (WT) or Rab27b Thr23Asn mutant, a dominant negative form of Rab27b, in COS7 cells (Supplementary Fig. 5). In all tested combinations, no co-immunoprecipitation of EGFP-Rab27b with HA-Rab27b could be observed. In contrast, as a positive control, EGFP-Rab27b WT was clearly co-immunoprecipitated with the HA-tagged effector granuphilin (residues 1–300).

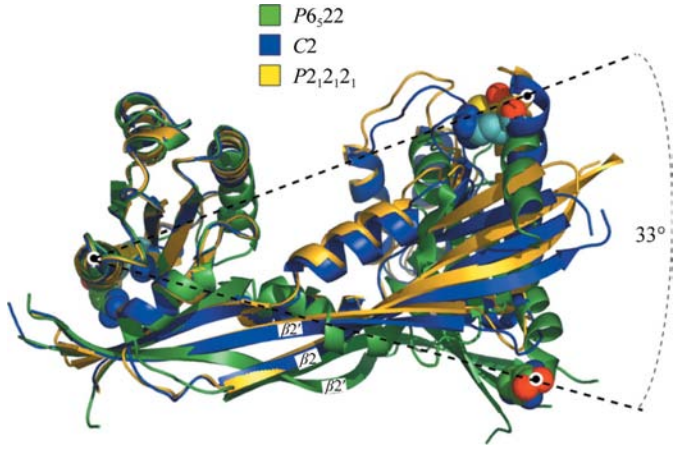


**Figure 7**
Flexibility of domain arrangements in the dimers. Superimposition of the core domains of molecules HA (green), MA (blue) and PA (yellow). The relative positions of the B molecules (right-hand side) in the respective dimers are tilted by 33° owing to variations in the switch I region. The angle was calculated by comparing the positioning of Arg184 (drawn as a space-filling model) in each monomer. Molecules are represented as ribbon models. The $\beta2$ strands belonging to molecules A and B are labelled $\beta2$ and $\beta2'$, respectively.

Unable to observe dimerized Rab27b–GDP by pull-down assays, we next performed dynamic light-scattering (DLS) studies of the protein in solution, which showed two scattering peaks with a 7:3 ratio (Supplementary Fig. 6). The main peak at 2.85 nm is consistent with the hydrodynamic diameter calculated from the structure of the monomeric core of Rab27b. The second peak at 59.4 nm could arise from soluble aggregates in the concentrated solution, but it does not correspond to a dimeric form of the GTPase. Additionally, small-angle X-ray scattering (SAXS) measurements were performed to confirm the oligomeric state of Rab27b–GDP. Because the sample aggregated at high concentration, SAXS experiments were carried out with low protein concentrations up to 5.56 mg ml$^{-1}$. Using Guinier analysis [Guinier plots and the concentration-dependence of $I(0)$/concentration and $R_g^2$ are shown in Figs. 8*a*, 8*b* and 8*c*], the apparent molecular weight (MW) and the radius of gyration ($R_g$) of the enzyme were determined to be 21.9 $\pm$ 0.8 kDa and 19.5 $\pm$ 0.6 Å, respectively. The calculated MW of Rab27b was almost identical to the theoretical value for the monomer structure (21.04 kDa), indicating that Rab27b–GDP is monomeric in solution. To further characterize the solution structure of the GTPase, three distinct $R_g$ values of Rab27b–GDP were assessed based on the coordinates from the three crystal structures: the Rab27b–GDP dimer (25.4 Å), an open monomer extracted from the dimer (18.3 Å) and a closed monomer deduced from other Rab GTPase structures (17.7 Å). The experimental $R_g$ of 19.5 Å is close to that predicted for the open monomer. Moreover, the calculated pair correlation function $P(r)$ is similar to that of the open monomer rather than those of the dimer or the closed monomer, with almost identical $D_{max}$ values (Fig. 8*d*). Taken together, these data do not provide physiological evidence for a functional dimer of Rab27b–GDP, at least in our biochemical experiments. Furthermore, the SAXS data suggest that Rab27–GDP might take a monomeric form with an elongated conformation in solution, rather than a compact closed form.

### 3.5. Nucleotide-binding site

The electron densities of GDP in the three space groups were clear, without density for a $\gamma$-phosphate (inset in Supplementary Fig. 1). The bound GDP lies in the nucleotide-binding pocket, interacting with one $Mg^{2+}$ ion (or possibly $Ca^{2+}$ ion in the case of the *C*2 space group, as its crystallization solution contains a 20-fold excess of calcium over magnesium) and 12 residues (Asp17, Gly19, Val20, Gly21, Lys22, Thr23, Thr24, Asn133, Lys134, Asp136, Ala164 and Ala165) which

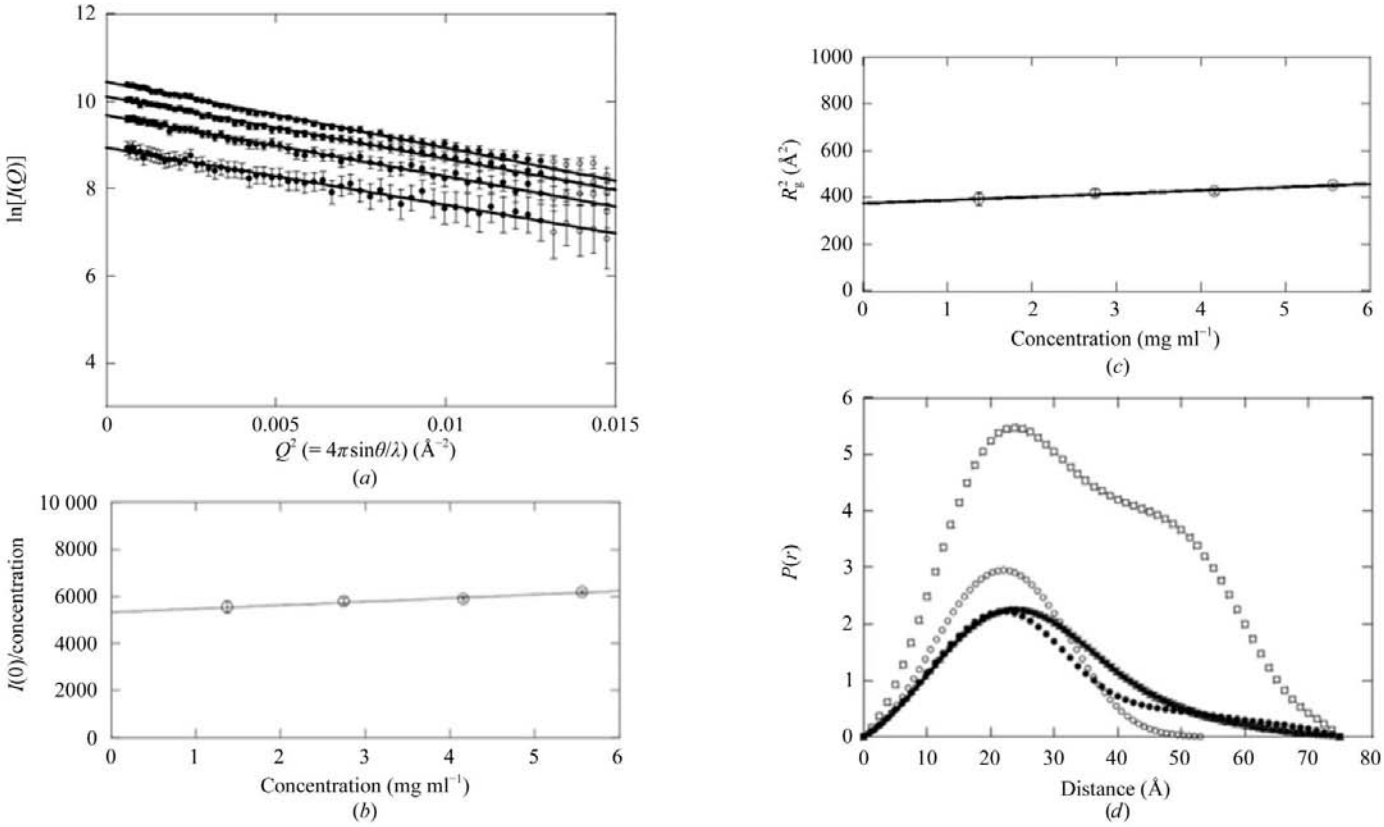


**Figure 8**
SAXS experiments. (*a*) Guinier plot of Rab27b–GDP. The plots were obtained from Rab27b concentrations of 1.37, 2.75, 4.16 and 5.56 mg ml$^{-1}$ from bottom to top. The dependence of $I(0)$/concentration and $R_g^2$ on the protein concentration are shown in (*b*) and (*c*), respectively. These values slightly increased with protein concentration, owing to interparticle interference. (*d*) Distance-distribution functions of Rab27–GDP in solution (solid line with error bars), in addition to various structural models derived from the crystal structures: Rab27b–GDP dimer (squares), open monomer extracted from the dimer (filled circles) and closed monomer deduced from other Rab GTPase structures (open circles).The calculation was performed by fitting the scattering profiles, scaled by $I(0)$, of Rab27b–GDP in solution to those of the monomer forms deduced from the crystal structures.

are highly conserved among GTPases (Fig. 1). The GDP binding is assured by both electrostatic and hydrogen-bonding interactions, with additional hydrophobic contacts with the base moiety. Thr41 of Rab27b, which further coordinates $Mg^{2+}$ in other GTP-form Rabs, is at a distance of ∼14 Å from the ion and is entangled in the swapping interface. The nucleotide-binding pocket is located far from the switch regions and is not involved in the swapped dimerization. Although the current resolution of the data does not allow a precise measurement of the distances between the active-site residues and the nucleotide atoms, the average values of the hydrogen-bond distances involved in the coordination of GDP are comparable to those of other GTPases (data not shown).

### 3.6. Disulfide bonding

When the $P6_522$, $C2$ and $P2_12_12_1$ structures are juxtaposed, an additional disparity is observed. In the monoclinic and orthorhombic structures, the $\alpha3$–$\beta5$ loop and the C-terminal region of helix $\alpha5$ are bridged by a disulfide bond between Cys123 and Cys188 (Fig. 9). In contrast, this bridge is missing in the hexagonal model. The cause of the differences between the three structures remains unclear, but might be ascribed to the oxidative status of the protein prior to crystallization: while the $P6_522$ crystals grew in the presence of reductant within 4 d, the $C2$ and $P2_12_12_1$ crystals appeared after several months. Interestingly, such folding is also present in the crystal structure of Cdc42–GTP, where a disulfide bond bridges the $\alpha3$–$\beta5$ loop with an extended C-terminal segment (Cys105–Cys188 in PDB entry 1nf3). The Cys123–Cys188 bond in Rab27b influences the orientation of the $\alpha3$ helix, the $\alpha3$–$\beta5$ loop and the $\alpha5$ helix. In the $P6_522$ crystal, $\alpha3$ shifts by up to 18° when compared with the other two structures (Fig. 9), also showing a different conformation (molecule HA) or the absence of electron density for the $\alpha3$–$\beta5$ loop and the $\alpha5$ N-terminus (molecule HB). Notably, a protein construct of residues 1–187, lacking Cys188, did not crystallize, even though the protein was still soluble and well folded (data not shown).

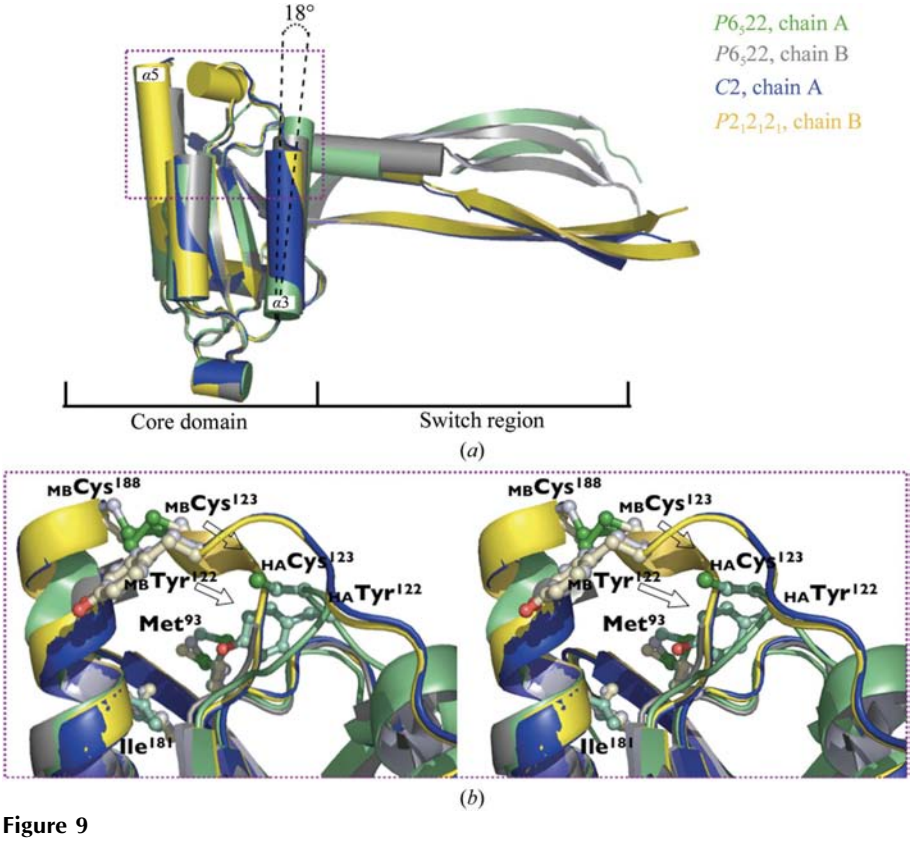


**Figure 9**
Variations in switch orientation. (*a*) Superimposition of Rab27b HA (green), HB (grey), MA (blue) and PA (yellow) molecules, represented as ribbon diagrams. Except for helix $\alpha3$, which shifts by about 18°, the core domains fit very well (within an r.m.s.d. of 0.75 Å), whereas the switch regions are present in different orientations. (*b*) highlights the disulfide bond in Rab27b in stereo. Cysteines forming the S–S bridge and conserved residues corresponding to the rabphilin 3A-recognizing residues of Rab3a are labelled and represented as a ball-and-stick model. The shifts of Tyr122 and Cys123 between the two lattices are emphasized by arrows.

## 4. Discussion

### 4.1. Swapping interface and nucleotide exchange

Domain-swapping occurs when fragments of one monomer trade with those of another monomer to create a dimer or higher oligomer and all subunits adopt a similar global structure that is comparable to the single monomer (Bennett *et al.*, 1994, 1995; Liu & Eisenberg, 2002). To date, this mechanism of oligomerization has been reported in association with several biological functions such as protein aggregation (Fink, 1998), protein misfolding leading to amyloid formation (Liu *et al.*, 2001) and the structural framework of some viruses (Qu *et al.*, 2000). The phenomenon is still rare and has mostly been reported for the exchange of N- or C-terminal polypeptides, with a few exceptions in which swapped domains are positioned in the middle of the protein (Liu & Eisenberg, 2002). Converting a monomer into a domain-swapped dimer implies folding/unfolding dynamics of the molecules, as both intertwined and single forms are energetically metastable, depending on the number of interactions and the compatibility of the interfaces between the swapped regions (Ding *et al.*, 2006). For secondary-structural elements to become intertwined, it is necessary to partially unfold the native structure of the monomer. In extreme cases, protein unfolding can lead to insoluble aggregates and loss of biological activity. The free-energy difference associated with monomer/dimer (or oligomer) equilibrium is relatively high (Rousseau *et al.*, 2003). The resulting kinetic barrier

should be crossed by a slow interconversion between monomeric and oligomeric states. Although various hypotheses have been put forth to explain the biological significance of domain-swapping, several domain-swapped structures have been attributed to an artifact of crystallization conditions (Liu & Eisenberg, 2002).

No dimerization of Rab27b was observed in solution by our gel-filtration, pull-down, DLS and SAXS experiments. However, as the SAXS data suggest an extended conformation of Rab27b in solution rather than the canonical compact structure, we cannot exclude the possibility of dimerization *in vivo* in locally crowded areas on the membranes where geranylgeranylated Rab27b localizes. Dimer formation of Rab GTPases in crystals, although without swapping, has also been observed in Rab9a–GDP (Wittmann & Rudolph, 2004) and Rab11a–GDP (Pasqualato *et al.*, 2004). In these structures, the GTPases adopt a folding that is similar on the whole to those of other small GTPases, with the exception of the $\beta$2 strands, which make contacts with the neighbouring molecule through the formation of an intermolecular $\beta$-sheet. This interaction was suggested to be the mechanism for negative regulation of GTPases. The inactive dimer of membrane-associated Rabs may not be able to recycle to the cytosol, but rather stays on the membrane as a pool of the inactive form. Indeed, the swapped dimer of Rab27b–GDP would not allow interaction with RabGDI because of a steric clash when the core structure of the Rab27b–GDP dimer is superimposed with that of Ypt1 in complex with RabGDI (Pylypenko *et al.*, 2006; data not shown). All the three structures ($P6_522$, $C2$ and $P2_12_12_1$ structures), with different relative orientations between protomers (Fig. 9), are incompatible with making a complex with RabGDI, suggesting that the Rab27b dimer would not interact with RabGDI, despite the possible conformational changes and plasticity of the dimeric Rab27b.

Upon GTP binding, the switch I, switch II and interswitch regions adjust their conformation to create an interface to mediate effector recognition. On the other hand, the GDP-bound structures show variable arrangements in the switch regions (Eathiraj *et al.*, 2005). In the swapped dimer of Rab27b–GDP, the switch I and switch II regions deviate substantially from the canonical positions and are used as hinge loops for domain swapping. Assuming that the GTP-activation of Rab27b restructures the switch regions, this alteration from the GDP-form to the GTP-form would thereby have to disrupt the swapping elements. Considering the necessity of flexibility of the switch elements to fulfil their role in the regulation of effector interaction and taken together with the variable conformations of the swapping $\beta$2 strand in the $P6_522$, $C2$ and $P2_12_12_1$ structures, it seems likely that the domain-swapping observed in the inactive Rab27b–GDP structures is a manifestation of the stabilization of intrinsically flexible switch regions.

Rab switches from the GDP-bound to the GTP-bound form with the assistance of GEF through various mechanisms depending on the GEF subfamily (Esters *et al.*, 2001). MSS4/DSS4 represents one GEF subfamily that is highly expressed in brain tissue; it triggers guanine-nucleotide exchange on a variety of Rabs, in contrast to the other substrate-specific RabGEFs. The recent crystal structure of the complex between Rab8a and MSS4 revealed a new process for nucleotide exchange through the unfolding and stabilization of the switch I and interswitch regions and the opening of the nucleotide-binding pocket (Itzen *et al.*, 2006). Both the partially unfolded Rab8a in complex with MSS4 and the open conformation of Rab27b–GDP tend to support a regulatory mechanism of these small GTPases by stabilizing their unfolded states. Assuming that the flexible switch I, switch II and interswitch regions of the GDP-form Rabs would easily switch between open and closed conformations, external factors such as other partner protein(s) as seen for the Rab8a–MSS4 complex (Itzen *et al.*, 2006) or homodimerization as reported here might fulfil stabilization of the switch regions.

### 4.2. Disulfide bridge and effector recognition

Located in and around the switch regions, RabFs help partner proteins differentiate between the GDP- and GTP-bound conformations, while RabSFs play key roles in the specific recognition of partners. The complex structure between Rab3a and rabphilin 3A revealed that conserved hydrophobic residues such as Met96, Trp125 and Ile183 of Rab3a recognize the SGAWFF structural element of the effector (Ostermeier & Brunger, 1999). These three residues belong to RabF4, RabSF3 and RabSF4 and correspond to Met93, Tyr122 and Ile181 in the Rab27 proteins, respectively. An induced-fit conformational change of the Rab3a $\alpha$3–$\beta$5 loop at the interface with the SGAWFF motif of rabphilin 3A places Rab3a Trp125 in its bound conformation (Ostermeier & Brunger, 1999). In the Rab27b GDP-bound form, the orientation of the corresponding Tyr122 of Rab27b in the $\alpha$3–$\beta$5 loop depends on the oxidation state of Cys123 and Cys188 (Fig. 9). Because the SGAWFF structural element is also well conserved in Rab27 effectors, the intramolecular disulfide-bond formation in Rab27b induced by oxidative stress might alter its interaction with effector proteins (Fig. 9). Of all the Rab structures solved to date, the present structure is the first example that exhibits an intramolecular S—S bond. Indeed, disulfide bridges are rarely found in cytosolic proteins because of the reductive environment in the cytosol. Structural analysis of Rab27a/b with their effectors would be a prerequisite to debate the status of the disulfide bridge as a potential method of functional regulation.

We thank the Photon Factory beamline staff for their assistance during the diverse data-acquisition procedures. This work was supported in part by the Protein 3000 project and by Grants-in-Aid from the Ministry of Education, Culture, Sports, Science and Technology of Japan.

## References

Bennett, M., Choe, S. & Eisenberg, D. (1994). *Protein Sci.* **3**, 1444–1463.

Bennett, M., Schlunegger, M. & Eisenberg, D. (1995). *Protein Sci.* **4**, 2455–2468.

Brünger, A. T., Adams, P. D., Clore, G. M., DeLano, W. L., Gros, P., Grosse-Kunstleve, R. W., Jiang, J.-S., Kuszewski, J., Nilges, M., Pannu, N. S., Read, R. J., Rice, L., Simonson, T. & Warren, G. L. (1998). *Acta Cryst.* D**54**, 905–921.
DeLano, W. (2005). *Drug Discov. Today*, **10**, 213–217.
Ding, F., Prutzman, K., Campbell, S. & Dokholyan, N. (2006). *Structure*, **14**, 5–14.
Dirac-Svejstrup, A., Sumizawa, T. & Pfeffer, S. (1997). *EMBO J.* **16**, 465–472.
Eathiraj, S., Pan, X., Ritacco, C. & Lambright, D. (2005). *Nature (London)*, **436**, 415–419.
Emsley, P. & Cowtan, K. (2004). *Acta Cryst.* D**60**, 2126–2132.
Esters, H., Alexandrov, K., Iakovenko, A., Ivanova, T., Thomä, N., Rybin, V., Zerial, M., Scheidig, A. & Goody, R. (2001). *J. Mol. Biol.* **310**, 141–156.
Fink, A. (1998). *Fold. Des.* **3**, 9–23.
Fukuda, M. (2005). *J. Biochem. (Tokyo)*, **137**, 9–16.
Itzen, A., Pylypenko, O., Goody, R., Alexandrov, K. & Rak, A. (2006). *EMBO J.* **25**, 1445–1455.
Izumi, T., Gomi, H., Kasai, K., Mizutani, S. & Torii, S. (2003). *Cell Struct. Funct.* **28**, 465–474.
Kawasaki, M., Nakayama, K. & Wakatsuki, S. (2005). *Curr. Opin. Struct. Biol.* **15**, 681–689.
Liu, Y. & Eisenberg, D. (2002). *Protein Sci.* **11**, 1285–1299.
Liu, Y., Gotte, G., Libonati, M. & Eisenberg, D. (2001). *Nature Struct. Biol.* **8**, 211–214.
Matthews, B. (1968). *J. Mol. Biol.* **33**, 491–497.
Nicholls, A., Bharadwaj, R. & Honig, B. (1993). *Biophys. J.* **64**, A166.
Ostermeier, C. & Brunger, A. T. (1999). *Cell*, **96**, 363–374.
Otwinowski, Z. & Minor, W. (1997). *Methods Enzymol.* **276**, 307–326.
Pan, X., Eathiraj, S., Munson, M. & Lambright, D. (2006). *Nature (London)*, **442**, 303–306.
Pasqualato, S., Senic Matuglia, F., Renault, L., Goud, B., Salamero, J. & Cherfils, J. (2004). *J. Biol. Chem.* **279**, 11480–11488.
Pereira-Leal, J. & Seabra, M. (2000). *J. Mol. Biol.* **301**, 1077–1087.
Pfeffer, S. (2005). *J. Biol. Chem.* **280**, 15485–15488.
Potterton, E., Briggs, P., Turkenburg, M. & Dodson, E. (2003). *Acta Cryst.* D**59**, 1131–1137.
Pylypenko, O., Rak, A., Durek, T., Kushnir, S., Dursina, B., Thomae, N., Constantinescu, A., Brunsveld, L., Watzke, A., Waldmann, H., Goody, R. & Alexandrov, K. (2006). *EMBO J.* **25**, 13–23.
Qu, C., Liljas, L., Opalka, N., Brugidou, C., Yeager, M., Beachy, R., Fauquet, C., Johnson, J. & Lin, T. (2000). *Structure*, **8**, 1095–1103.
Rak, A., Fedorov, R., Alexandrov, K., Albert, S., Goody, R., Gallwitz, D. & Scheidig, A. (2000). *EMBO J.* **19**, 5105–5113.
Rak, A., Pylypenko, O., Niculae, A., Pyatkov, K., Goody, R. & Alexandrov, K. (2004). *Cell*, **117**, 749–760.
Rousseau, F., Schymkowitz, J. & Itzhaki, L. (2003). *Structure*, **11**, 243–251.
Seabra, M., Mules, E. & Hume, A. (2002). *Trends Mol. Med.* **8**, 23–30.
Svergun, D., Barberato, C. & Koch, M. H. J. (1995). *J. Appl. Cryst.* **28**, 768–773.
Svergun, D. I. & Stuhrmann, H. B. (1991). *Acta Cryst.* A**47**, 736–744.
Terwilliger, T. & Berendzen, J. (1999). *Acta Cryst.* D**55**, 849–861.
Verhoeven, K., DeJonghe, P., Coen, K., Verpoorten, N., Auer-Grumbach, M., Kwon, J. M., FitzPatrick, D., Schmedding, E., DeVriendt, E., Jacobs, A., Van Gerwen, V., Wagner, K., Hartung, H. P. & Timmerman, V. (2003). *Am. J. Hum. Genet.* **72**, 722–727.
Wittmann, J. & Rudolph, M. (2004). *FEBS Lett.* **568**, 23–29.
Wu, M., Wang, T., Loh, E., Hong, W. & Song, H. (2005). *EMBO J.* **24**, 1491–1501.
Zerial, M. & McBride, H. (2001). *Nature Rev. Mol. Cell Biol.* **2**, 107–117.
Zhang, H., Seabra, M. & Deisenhofer, J. (2000). *Structure*, **8**, 241–251.
Zhao, S., Torii, S., Yokota-Hashimoto, H., Takeuchi, T. & Izumi, T. (2002). *Endocrinology*, **143**, 1817–1824.
Zhu, G., Zhai, P., Liu, J., Terzyan, S., Li, G. & Zhang, X. (2004). *Nature Struct. Mol. Biol.* **11**, 975–983.